
Article:
Mufundirwa, A., Harrington, G.F., Ismail, M.S. et al. (7 more authors) (2020) Gram-scale synthesis of alkoxide-derived nitrogen-doped carbon foam as a support for Fe-N-C electrocatalysts. Nanotechnology, 31 (22). 225401. ISSN 0957-4484

https://doi.org/10.1088/1361-6528/ab76ed

Gram-scale synthesis of alkoxide-derived nitrogen-doped carbon foam as a support for Fe-N-C electrocatalysts

To cite this article before publication: Albert Mufundirwa *et al* 2020 *Nanotechnology* in press https://doi.org/10.1088/1361-6528/ab76ed

Gram-Scale Synthesis of Alkoxide-Derived Nitrogen-Doped Carbon Foam as a Support for Fe-N-C Electrocatalysts

Albert Mufundirwa[a], George F. Harrington[b], Mohammed S. Ismail[c], Břetislav Šmid[d,e], Benjamin V. Cunning[d,f], Yu Shundo[d], Mohamed Pourkashanian[c], Kazunari Sasaki[a,b,d], Akari Hayashi[a,g], and Stephen M. Lyth[c, d, g*]

[a] *Department of Hydrogen Energy Systems, Faculty of Engineering, Kyushu University, 744 Motooka, Nishi-ku, Fukuoka 819-0395 Japan*

[b] *Next-Generation Fuel Cell Research Center (NEXT-FC), Kyushu University, 744 Motooka, Nishi-ku, Fukuoka 819-0395 Japan*

[c] *Energy2050, Department of Mechanical Engineering, Faculty of Engineering, University of Sheffield, Ella Armitage Building, Sheffield, S3 7RD, United Kingdom*

[d] *International Institute for Carbon-Neutral Energy Research (WPI-I2CNER), Kyushu University, 744 Motooka, Nishi-ku, Fukuoka 819-0395 Japan*

[e] *Faculty of Mathematics and Physics, Department of Surface and Plasma Science, V Holešovičkách 2, 18000, Charles University in Prague, Czech Republic*

[f] *Center for Multidimensional Carbon Materials, Ulsan National Institute of Science and Technology (UNIST), Ulsan, 89-798, Republic of Korea*

[g] *Platform of Inter/Transdisciplinary Energy Research, Kyushu University, 744 Motooka, Nishi-ku, Fukuoka 819-0395 Japan*

[*]Corresponding author: Tel: 092 802 6742 Email: lyth@i2cner.kyushu-u.ac.jp

Abstract

Non-platinum group metal (non-PGM) catalysts for the oxygen reduction reaction (ORR) are set to reduce the cost of polymer electrolyte membrane fuel cells (PEFCs) by replacing platinum at the cathode. We previously developed unique nitrogen-doped carbon foams by template-free pyrolysis of alkoxide powders synthesized using a high temperature and high pressure solvothermal reaction. These were shown to be effective ORR electrocatalysts in alkaline media. Here, we present a new optimised synthesis protocol which is carried out at ambient temperature and pressure, enabling us to safely increase the batch size to 2 g, increase the yield by 60%, increase the specific surface area to 1866 m^2/g, and control the nitrogen content (between 1.0 and 5.2 at%). These optimized nitrogen-doped carbon foams are then utilized as effective supports for Fe-N-C catalysts for the ORR in acid media, whilst multiphysics modelling is used to gain insight into the electrochemical performance. This work highlights the importance of the properties of the carbon support in the design of Pt-free electrocatalysts.

Keywords: oxygen reduction reaction; ORR; non-PGM, platinum-free; nitrogen-doped carbon; Pt-free; catalyst support; Fe-N-C; template-free

1. Introduction

The platinum cathode catalyst contributes significantly to the high cost of polymer electrolyte membrane fuel cells – up to 45% of the stack cost by some estimates.[1] Research into alternative Pt-free catalysts for the oxygen reduction reaction (ORR) has been underway for decades.[2] The most promising non-precious catalysts are transition metal-containing nitrogen-doped carbon materials, generally synthesized by pyrolysis of various mixtures of iron, nitrogen, and carbon precursors. It is well-established that the final performance of such catalysts is dependent on a wide variety of different factors, including the proportions and ratios of the different elements, the atomic configuration of these elements, and in particular, the chemical environment of nitrogen and transition metal species in the carbon matrix. [3–11] In addition, other factors such as conductivity and microstructure also play an important role. All of the above factors can vary significantly depending on the type and ratio of precursors used, the pyrolysis temperature, the rate of heating during pyrolysis, the gases used in pyrolysis, and the type of support used.[12–18]

Carbon is a commonly used support material for electrocatalysts. It can be synthesized to have very large surface area and controllable porosity, providing suitable passageways for diffusion of reactants and products.[19,20] Carbon is relatively chemically inert, making

it resistant to many reactive species, and improving its durability in electrochemical devices.[21] Carbon has good electrical conductivity, helping to minimize electrode resistance and increasing the efficiency for fuel cell applications.[22] An enhanced understanding of the fundamental principles behind the synthesis process of carbon-based catalysts will enable development of better synthesis protocols and improved ability to scale-up production.

Here we employ a specific type of carbon foam derived from the decomposition of metal alkoxide powders as a support material for Fe-N-C catalysts. The advantage of this class of carbon foam is that it can be synthesized without the need for a sacrificial template, it has very large surface area (up to 3000 m^2/g), relatively large pore-size (>1 μm), can be produced at multi-gram scale, and as a "bottom-up" technique the chemical structure can be routinely modified.[23] This type of carbon foam was first synthesized by Choucair et al., by solvothermal reaction between sodium and ethanol, followed by pyrolysis.[24] We (and other researchers) showed that the solvothermal step was not required, that such carbon foams can be formed simply through pyrolysis of sodium ethoxide powder, and that it had applications such as hydrogen storage, due to the large surface area.[25–27] Later we showed that superhydrophobic fluorinated carbon foam can be synthesized by

replacing ethanol with e.g. trifluoroethanol.[28] Similarly, we synthesized nitrogen-doped carbon foams by replacing ethanol with e.g. ethanolamine.[12] We went on to utilize such nitrogen-doped carbon foams to gain insight into the ORR in metal-free (or "no metal added") non-platinum group metal (non-PGM) catalysts.[13,29,30] The nitrogen content can be controlled by changing the amount and the type of nitrogen-source in the reaction, e.g. by using varying ratios of ethanol with either ethanolamine, diethanolamine, or triethanolamine.

Here, we attempt to simplify and scale up the production of nitrogen-doped carbon foams by switching synthesis of the precursor alkoxide powder from a high temperature and high pressure solvothermal reaction (Method A), to a new ambient temperature and ambient pressure, solution-based reaction protocol (Method B). This change means that scaling up the reaction can be achieved more safely, and the costs of synthesis can be significantly reduced. We perform several optimization steps with the specific aim of increasing the surface area, increasing the yield, controlling the nitrogen content, finally using these tailored nitrogen-doped carbon foams as supports for effective Fe-N-C catalysts.

2. Experimental

The catalyst precursors used in this study were synthesized via two different methods (Figure 1a, b). In the "solvothermal method" previously employed by our group (and others) (**Method A**), anhydrous ethanol (EtOH, Wako) and triethanolamine (TEOA, Aldrich) were added to a polytetrafluoroethylene-lined (PTFE-lined) high-pressure reactor (50 ml, Flon Industry, Japan), followed by an equimolar amount of sodium lumps (Aldrich). The reactor was quickly sealed, and then heated to 150 °C for 24 hours. After this, the vessel was cooled to room temperature and opened. Owing to additional safety concerns of high pressure, extra care was given to the sealing and opening of the reactor. The resulting nitrogen-containing sodium alkoxide powder was removed, dried under vacuum, and crushed in a pestle. Three different types of precursor were synthesized using Method A, by changing the TEOA:EtOH ratio from 1:1 to 1:3 to 1:9, in order to vary the nitrogen content.

The new solution-based synthesis protocol (**Method B**) is designed to be more scalable, lower cost, and safer than Method A. The key difference is the use of the solvent tetrahydrofuran (THF, Wako), slowing down the reaction rate by decreasing the concentration of the reactants. A two-neck flat-bottom flask (300 ml) was used. First, air

was evacuated from the flask using a roughing pump, and then N_2 gas flow was introduced through one of the necks. For safety, the reaction vessel was initially cooled using an ice bath. THF, EtOH and TEOA were introduced into the flask by pipette, and magnetically stirred, still under flowing N_2. Finally, sodium lumps were added. The ice bath was removed once the reaction was confirmed to proceed steadily. After 72 hrs the sodium lumps had completely reacted with the EtOH and TEOA, leaving a yellow-brown sodium alkoxide solution. This was dried in a rotary evaporator to recover the THF and obtain a yellow-white alkoxide powder, which was then crushed in a pestle.

The powdery sodium alkoxide precursors resulting from Method A and Method B were first heat treated in a box furnace at 600 ˚C for 2 hours, under nitrogen flow (75 ml/min), to form the carbonaceous product. The heating rate of this first "structure forming" step was either 2, 5, or 10 ˚C/min. The heating conditions are described in Table 1. This carbonized product was then stirred overnight in deionized water, washed five times using vacuum filtration (to remove sodium-containing impurities), and then dried at 80 °C under vacuum. The powders were then subjected to a second pyrolysis step under nitrogen, at either 900 or 1000 ˚C for 2 hours (75 ml/min, 5 °C/min). The nitrogen-doped carbon (N-C) derived from Method A is labelled N-C-A$(x{:}y)_{r,T}$, where *A* denotes Method A; *x*:*y* is the ratio TEOA:EtOH; *r* is the heating-rate during the first "structure-forming"

pyrolysis step (either 2, 5 or 10˚C/min); and *T* is the temperature of the second pyrolysis step. Likewise the materials derived from Method B are labelled N-C-B(x:y)$_{r,T}$. The TEOA:EtOH ratio and heat treatment conditions for Method B were selected based on the most favorable results obtained using Method A. The Fe-N-C catalyst was then prepared using iron (II) acetate as an iron source (FeAc, Tokyo Chemical Industry), adsorbed onto the carbon foam catalyst support deemed most suitable according to the preceding characterization. As such, 100 mg of N-C-B (1:3)$_{5,1000}$ was added to 50 ml of water, 14.3 mg of FeAc was added to 10 ml of water, and then these two solutions were mixed together and magnetically stirred for 2 hrs. This mixture was then vacuum filtered once to remove excess FeAc, dried under vacuum, and then heat-treated in a tube furnace under flowing NH_3:N_2 (1:19, 100 ml/min) at 900 ˚C, for 2 hours. Table 1 summarizes the synthesis conditions and comparison of different properties for all nitrogen-doped carbon samples used in this study.

The resulting materials were characterized by field emission scanning electron microscopy (FE-SEM, Hitachi S-500 / FE-SEM, JEOL JSM-7001F); Brunauer Emmet and Teller (BET) and Barrett Joyner and Halenda (BJH) nitrogen adsorption surface area analysis (3 Flex Surface Characterization, Micromeritics); X-ray diffraction (XRD) with Cu Kα-radiation source (λ=1.54 Å, RINT-Ultima III, Rigaku Corp.); X-ray photoelectron

spectroscopy (XPS, PHI 5000 Versa probe (II), ULVAC); and transmission electron microscopy (TEM, JEM-2100HCKM, JEOL LTD., Japan).

An automated polarization system, rotating ring-disk electrode (RRDE) set-up, and a three-electrode electrochemical cell were used for characterization of the electrochemical properties of the catalysts (Hokuto Denko Corp.;, HR-500, and HX-107, respectively). A carbon rod counter electrode (Hokuto Denko Corp. Ø 6 mm x 150 mm) and an Ag/AgCl reference electrode (HX-RAg) were used. Electrocatalyst ink was made by dispersing the nitrogen-doped carbon foams (5 mg) in a mix of deionized water, ethanol and 5 wt.% Nafion dispersion, in a volume ratio of 3:3:1. The catalyst inks were then sonicated for 30 min using ultrasonic homogenizer (UH-600, SMT Co., Ltd.). The working electrode was then prepared by coating 8 µl of electrocatalyst ink onto the glassy carbon electrode, which was then dried at 60 ºC in air for 10 minutes. The loading density of catalyst on the electrode was 580 $\mu g_{catalyst}/cm^2$.

Electrochemistry was performed in O_2 or N_2 gas saturated 0.1 M $HClO_4$ electrolyte, at room temperature. Cyclic voltammograms (CVs) were measured with a scan rate of 50 mV s^{-1} in N_2-saturated solution. All voltages are written relative to the reversible hydrogen electrode (RHE). Linear sweep voltammograms (LSVs) were obtained between

0.05 to 1.2 V_{RHE}, at 10 mV s^{-1}, in O_2-saturated electrolyte solution at rotations of 400, 900, 1600, and 2500 rpm. For RRDE, LSVs were plotted after subtracting the current measured under nitrogen-saturation, and normalization of the minimum current density to zero. All of the CV and LSV results are shown after 50 break-in cycles, after the stabilization of the activity. Onset potentials were determined from first derivatives of the LSV data (Fig. S6). The mass activity was calculated using the kinetic current (i_k) obtained from the intercept of the Koutecky-Levich plot and total mass of catalyst (m): mass activity = i_k/m. Durability measurements were performed over 60,000 start-stop cycles according to previously established protocols.[13,31]

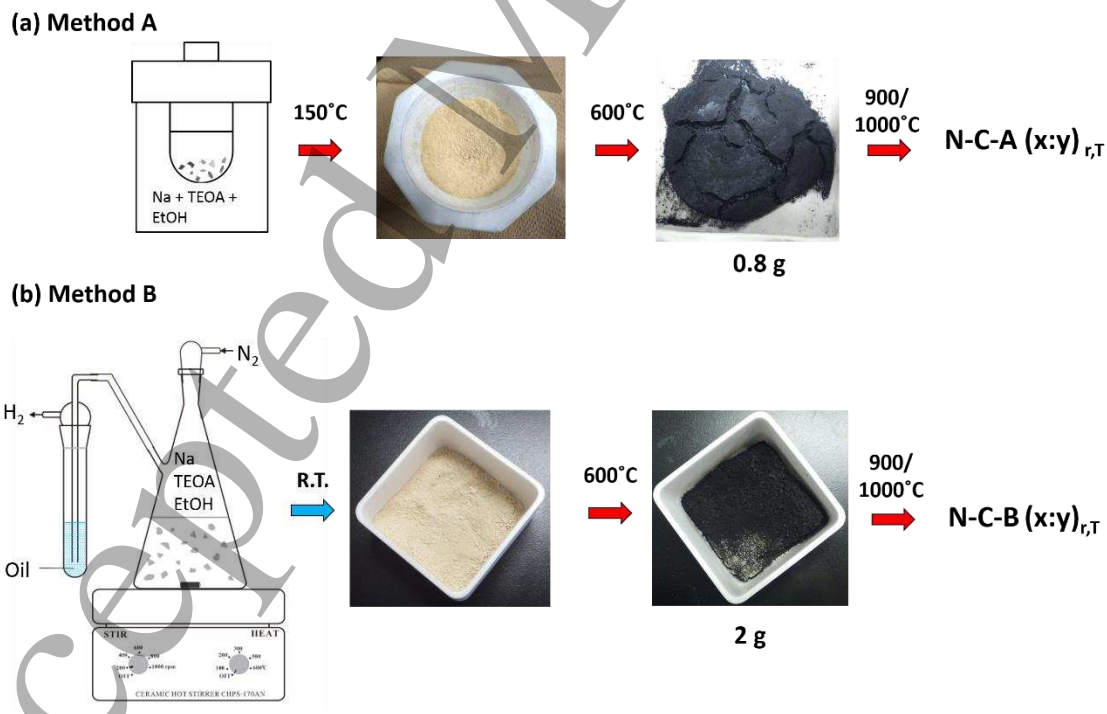

Figure 1: Different synthetic routes for production of nitrogen-doped carbon foams: (a) Method A (solvothermal synthesis at high temperature and pressure); and (b) Method B (solution synthesis under flowing nitrogen, at standard temperature and pressure).

3. Results and Discussion

3.1 Product Mass and Yield

Table 1 and Table S1 show the mass and yield of the carbon products synthesized using different methods and conditions. For Method A, the final product mass varies between 160 and 540 mg, whilst the yield varies from 0.8 to 3.1%. The low yield of 1.3 % at low TEOA ratio (1:9) may be attributed to the low concentration and strong basic nature of TEOA (pH = 10) in the precursor reactants, resulting in a slower rate of deprotonation compared to that of ethanol (pH = 7.3). The low yield at high TEOA ratio of 1:1 could be due to an increase in viscosity of the solution under these conditions, complicating the uniform deprotonation of TEOA and EtOH. The best yield and mass are obtained for the sample with a TEOA:EtOH ratio of 1:3 and therefore this ratio was selected for use in Method B.

Using Method B, the product mass increases to between 440 and 1200 mg, whilst the yield increases to between 2.5 and 7.0 %, compared with Method A. The overall increase in yield for Method B is largely attributed to the use of flowing nitrogen, preventing the formation of side-products through reaction between oxygen or humidity in the air with the sodium, due to temperature and kinetic effects. These results are a clear indication of the advantage of the new synthesis protocol, Method B. Notably, the sample formed with

a ramp rate of 5 °/min resulted in the highest yield, a significant improvement compared to heating rates of 2 and 10 °/min. This clearly indicates the importance of optimizing the heating rate for the second heat treatment step.

*Table 1: Summary of the synthesis conditions, product mass, yield, and surface area for the samples. *The product mass of the 2nd heat treatment step is inferred from the yield – the real value is approximately half of this, since the samples were divided for different heat treatment conditions.*

	TEOA: EtOH	1st Step Ramp Rate (°/min)	2nd Step Temperature (°C)	2nd Step Product Mass (g)*	Final Yield (%)	Final Surface area (m^2/g)	Sample Name
Method A	1:9	10	900	0.21	1.3	346	N-C-A(1:9)$_{10,900}$
	1:3		900	0.54	3.1	400	N-C-A(1:3)$_{10,900}$
			1000	0.53	3.0	351	N-C-A(1:3)$_{10,1000}$
	1:1		900	0.16	0.8	100	N-C-A(1:1)$_{10,900}$
Method B	1:3	10	900	0.61	3.5	1075	N-C-B(1:3)$_{10,900}$
			1000	0.58	3.3	813	N-C-B(1:3)$_{10,1000}$
		5	900	1.24	7.0	1500	N-C-B(1:3)$_{5,900}$
			1000	1.20	6.8	1286	N-C-B(1:3)$_{5,1000}$
		2	900	0.46	2.7	1866	N-C-B(1:3)$_{2,900}$
			1000	0.44	2.5	1620	N-C-B(1:3) $_{2,1000}$

3.2 Scanning Electron Microscopy (SEM)

Figure 2 shows SEM images of nitrogen-doped carbon foams synthesized using methods A and B, with different nitrogen-dopant ratios. The primary particle size is uniform at ~1 to 50 µm in all samples, which was achieved by simply grinding in a pestle, without energy intensive milling or sieving. All the samples have similar microstructure, with a 3-D foam-like carbon framework. This framework is highly porous, with large spheroidal voids ~2 µm in diameter in most cases. The walls of these cells are extremely thin, as evidenced by their electron transparency, even under low accelerating voltage SEM electron irradiation. It should be emphasized that this porous structure results from a completely template-free foaming process, eliminating the need to use a hard template, and thus significantly reducing the cost and number of processing steps.

Exclusively in the case of N-C-A(1:1)$_{10,900}$ (Figure 2(e, f)), solid-appearing spheroidal carbon structures are observed instead of the usual pores, but with similar diameter to the pores of the other samples. These are presumed to be hollow and to effectively be partially-formed pores. This provides some indirect evidence that the formation of these porous carbons is due to a foaming process during decomposition (this foaming can also be observed by eye if the samples are burned in air). The size of the "bubbles" formed

during the foaming process therefore determines the size of the pores after carbonization. In the specific case of N-C-A(1:1)$_{10,900}$, the TEOA ratio is relatively high, affecting the melting point and viscosity of the sodium alkoxide precursor. In this case, this seems to result in sealed hollow carbon nanoparticle bubbles, rather than the open porous structure of the other materials. We previously observed such hollow nanoparticles by transmission electron microscopy (TEM) in similar fluorinated carbon materials.[28] This unusual microstructure will probably affect properties such as surface area and mass diffusion, and this sample is therefore unlikely to be suitable for use as a catalyst or catalyst support. This also informed the decision to use an optimized TEOA:EtOH ratio of 1:3 for Method B, to maximize the nitrogen content in the final product whilst retaining the open porous network.

The materials synthesized using Method B (Fig. 2g-j) have similar particle size distribution and porous structure as those using Method A. This confirms that despite increasing the scale of production by ~60 %, and using a safer / less energy intensive process, the same general structure can be obtained. It also confirms the high reproducibility of materials produced using this technique, despite the different precursor ratios, pyrolysis conditions, and synthesis methods. The pore size in N-C-B(1:3)$_{5,1000}$ (Fig. 2 (i, j)) appears to be much smaller (i.e. ~250-500 nm) than in N-C-B(1:3)$_{2,1000}$ (Fig. 2 (g,

h)). This is attributed to the increase in heating rate in the first "structure-forming" step, again changing the way in which the sodium alkoxides precursor melts, foams and decomposes. Having smaller pores is expected to improve the volumetric activity of any resulting catalyst, and therefore is more desirable. Figure 3 shows a typical low-magnification SEM image of one of the catalysts. This also highlights the highly uniform and reproducible nature of the carbon powders synthesized using this technique.

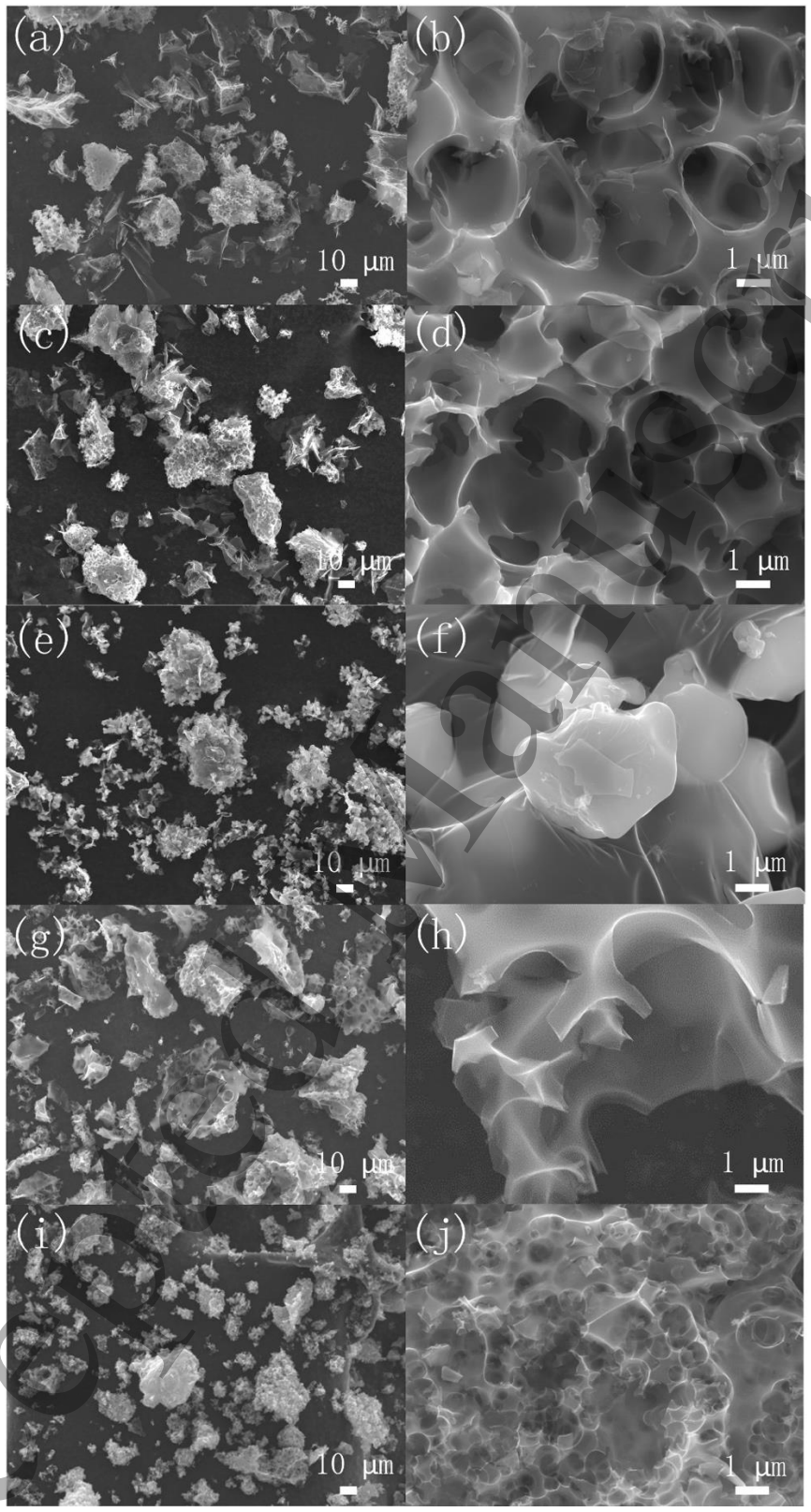

Figure 2: SEM images of: (a, b) N-C-A(1:9)$_{10,900}$; (c, d) N-C-A(1:3) $_{10,900}$; (e, f) N-C-A(1:1)$_{10,900}$; (g, h) N-C-B(1:3)$_{2,1000}$; and (i, j) N-C-B(1:3)$_{5,1000}$, at two different magnifications.

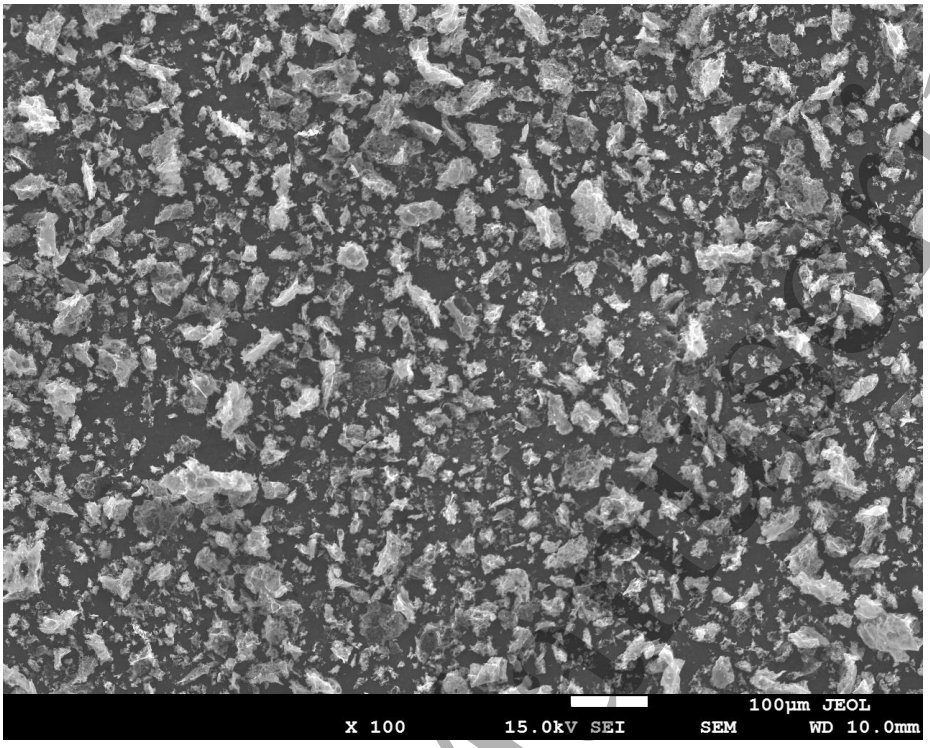

Figure 3: Low magnification SEM image of carbon foam catalyst sample N-C-B(1:3)$_{5,1000}$, which is representative of all the samples studied here.

3. 2 Surface Area and Porosity

The porosity and surface areas of the different nitrogen-doped carbon foams (Table 1) were determined from the adsorption/desorption isotherms in Figure 4 (a) and Figure S3. For Method A, the measured surface areas are 346, 400, 351 and 100 m^2g^{-1} (average: 299 m^2g^{-1}) for N-C-A(1:9)$_{10,900}$, N-C-A(1:3)$_{10,900}$, N-C-A(1:3)$_{10,1000}$, and N-C-A(1:1)$_{10,900}$, respectively. Despite the changing TEOA:EtOH ratio, the first three samples have similar surface area. However, N-C-A (1:1)$_{10,900}$ has significantly lower surface area, which is

attributed to the spherical closed-cell structures observed by SEM, preventing infiltration of nitrogen gas to the interior, and thus lowering the accessible surface area. In the case of the more open porous structures, nitrogen can access every surface. This further influenced the decision to use a ratio of 1:3 in Method B, to combine the relatively high nitrogen content with reasonable surface area.

The samples synthesized using Method B have a much higher average surface area of 1360 m^2g^{-1}. This clearly shows that Method B is an improved synthesis method. There is a trend of increasing surface area with decreasing ramp rate with average surface areas of 944, 1393, and 1743 m^2g^{-1} for ramp rates of 10, 5, and 2 °/min, respectively. This may be connected to the amount of time available for micropore formation during the carbonization process when a lower ramp rate is used. There is also a decrease in surface area when a higher temperature is used in the second pyrolysis step, which is commonly observed for carbon.

The International Union of Pure and Applied Chemistry (IUPAC) defines micropores as having pore diameters less than 2 nm; mesopores as having pore diameters between 2 and 50 nm; and macropores as having pore diameters greater than 50 nm. Most of the

isotherms here have Type I(a) characteristics, indicating microporous materials with narrow micropores (of <1 nm). The inflection at ~1 MPa indicates a Type II isotherm contribution, indicating non-porous or macroporous regions of the sample, which may correspond to the surfaces of the large micron-scale macropores observed by SEM.[32,33] In addition, Type H4 hysteresis loops are observed in the Method B samples, which indicate a micro-mesoporous nature, normally associated with micropore filling in micro-mesoporous carbons, providing further evidence of their micro-mesoporous nature. The exception is N-C-A(1:1)$_{10,900}$ which has a Type III isotherm associated with non-porous or microporous solids, reflecting the unusual closed-cell morphology as observed by SEM.[33,34]

The presence of micropores is supported by the MP method analysis shown in Figure 4 (b), where V_p is the pore volume, and r_p is the pore radius. The peak pore radius ranges from 0.65 to 0.80 nm in all cases. Method A results in lower micropore volume compared to Method B, in agreement with the lower BET surface area. In the case of N-C-A(1:1)$_{10,900}$ the micropore volume is very small, suggesting that nitrogen adsorption occurs mostly over the external surface area of the closed-cells,[34] in agreement with the Type II isotherm and the SEM images.

The BJH pore size distributions are plotted in Figure S4, highlighting the meso- and macropore ranges. The maximum observable pore size using this technique is ~100 nm, so the micron-scale macropores seen in the SEM images are not manifested in this data. The mesopore distribution is remarkably similar in all the samples. There is a small peak at a pore radius of ~35 nm in all cases. Meanwhile, the majority of pores have a radius of less than 10 nm, in agreement with the MP-plots.

In summary of the surface area and porosity data, these materials have broad distributions of micropores (highlighted by the MP method), mesopores (shown in the BJH data), and the macropores observed by SEM. Method B results in larger micro- and mesopore volume. Since the surface area, porosity, and pore connectivity have a significant influence on the accessibility of catalytic active sites, it is expected from the above results that Method B would be most suited to electrochemical applications.

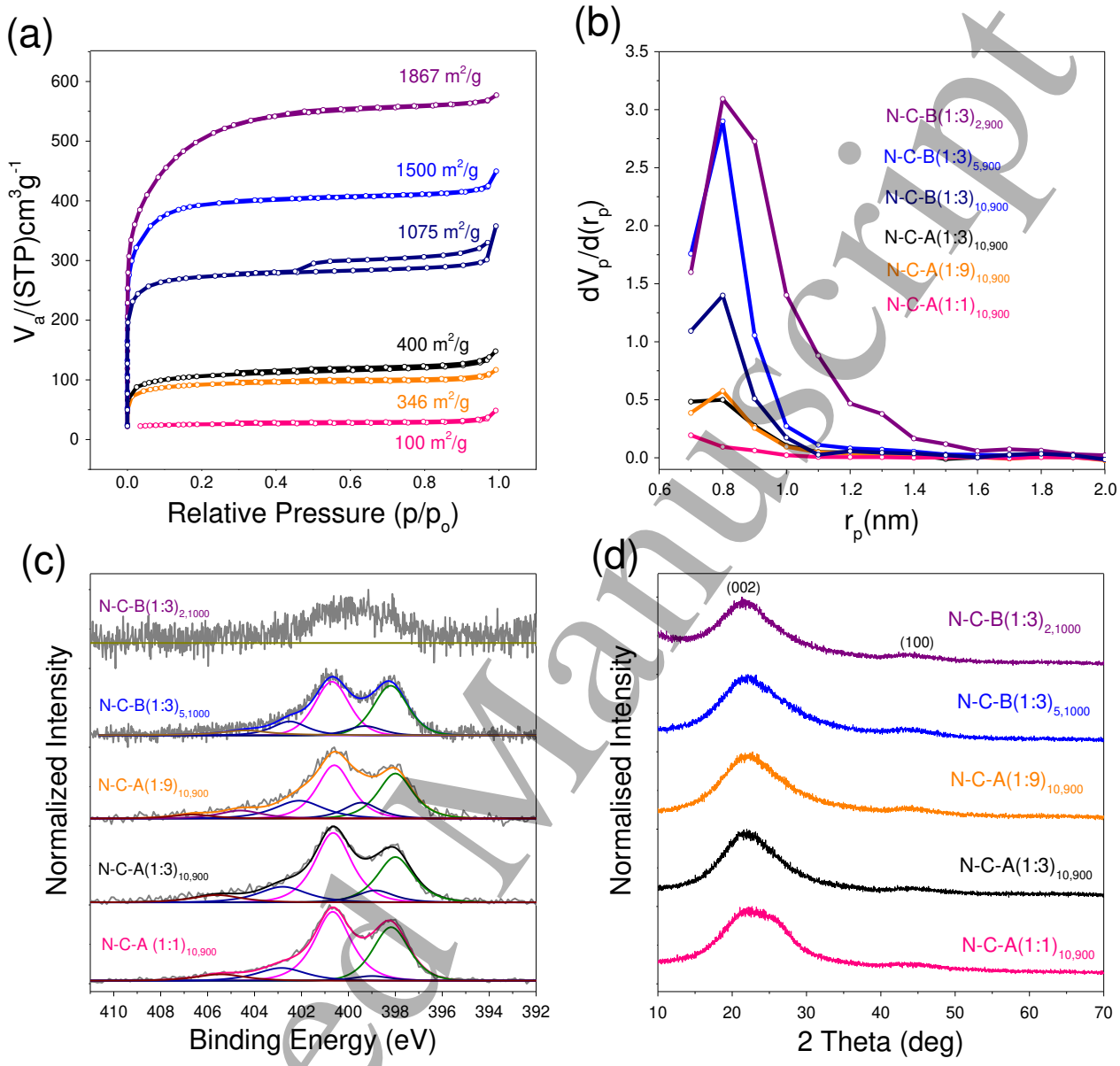

Figure 4: (a) BET surface area, (b) MP-plots, (c) normalized N 1s deconvolution of the XPS spectra, and (d) XRD spectra of the samples.

3.3. X-ray Photoelectron Spectroscopy (XPS)

Figure S1 shows XPS wide-scans of all the samples, and the elemental compositions are summarized in Table 2. The XPS surveys for all samples show a predominant C 1s peak at ~284.5 eV, an O 1s peak at ~532 eV, and an N 1s peak at ~398.2 eV. In the catalysts

synthesized using Method A, the final nitrogen content increases with increasing TEOA:EtOH ratio, from 2.0 to 2.9 to 4.3 wt%. This is as expected, correlating with the amount of nitrogen in the precursor, and showing that this synthesis method is suitable for tailoring the nitrogen-content of the carbon foams.

For Method B, the nitrogen content increases as the ramp rate increases (saturating at about 3.5 wt%), suggesting that more nitrogen is lost from the sample when the pyrolysis process is slower/longer, as expected. The oxygen content is significantly lower for Method B compared to Method A, suggesting that performing the reaction under nitrogen atmosphere helps to suppress the incorporation of oxygen-containing surface functional groups, and/or results in less adsorbed water on the surface (possibly due to enhanced hydrophobicity). There is a significant difference in residual sodium content depending on whether the second pyrolysis step is performed at 900 or 1000 ºC, for both Method A and Method B. This could be attributed to heating the sample to well above the boiling point of sodium (882.8 ºC); and/or the decomposition/reaction of residual NaOH and $NaCO_3$ to form Na and CO_2 at elevated temperature.

The pyrrolic, pyridinic, and graphitic C-N bonds observed in the deconvolution of the N 1s peak (Figure (4c)) confirm that nitrogen atoms were successfully doped into the carbon matrix. All the samples have remarkably similar profiles, further highlighting the reproducibility and consistency of these different synthesis protocols. Peak fitting mainly reveals the presence of pyridinic (~398.2 eV); pyrrolic (~399.3 eV), and graphitic / tertiary (400.8 eV) nitrogen, as well as oxygen-coordination peaks (> 402 eV).[35] The ratio of graphitic nitrogen to pyridinic nitrogen is 1.2 ± 0.2 in all cases. The one exception is N-C-B_2 (1:3), which has a much lower nitrogen content (attributed to the slower heating rate), resulting in a low signal to noise ratio, and thus preventing realistic peak fitting. The high proportion of pyridinic species in these samples are expected to provide suitable sites for Fe coordination in the final section of this study.

Table 2: XPS analysis of the materials used in this study after the 1st (black text) and 2nd (red text) pyrolysis steps.

Sample Name	XPS (wt. %)							
	C		N		O		Na	
	1st	2nd	1st	2nd	1st	2nd	1st	2nd
N-C-A(1:9)$_{10,900}$	73.5	73.7	3.7	2.0	19.2	21.3	3.6	3.0
N-C-A(1:3)$_{10,900}$	76.4	79.5	4.9	2.9	16.0	15.9	2.7	1.7
N-C-A(1:3)$_{10,1000}$	76.4	90.0	4.9	3.5	16.0	5.5	2.7	0.8
N-C-A(1:1)$_{10,900}$	62.8	65.9	6.3	4.3	24.6	22.1	6.3	7.7
N-C-B(1:3)$_{10,900}$	-	90.4	-	3.8	-	4.0	-	1.7
N-C-B(1:3)$_{5,900}$	72.5	77.8	6.7	5.2	14.9	11.0	5.9	5.9
N-C-B(1:3)$_{2,900}$	76.3	82.5	1.7	1.8	15.4	10.0	6.6	5.7
N-C-B(1:3)$_{10,1000}$	-	92.0	-	3.4	-	3.5	-	1.0
N-C-B(1:3)$_{5,1000}$	72.5	92.6	6.7	3.4	14.9	3.7	5.9	0.4
N-C-B(1:3)$_{2,1000}$	76.3	88.6	1.7	1.0	15.4	10.3	6.6	0.1

3.4 X-ray Diffraction (XRD)

Figure 4 (d) shows XRD spectra for the samples. These are all almost identical, with a broad diffraction peak at 22º, which corresponds to typical (002) interlayer spacing of 0.4 nm for amorphous or nitrogen-doped carbons[36,37]. A smaller peak centered at 44º is associated with the (100) in-plane hexagonal atomic arrangement of sp^2 carbon (i.e., 0.2 nm).

3.5 Electrochemical Characterization

In order to gauge the suitability of these nitrogen-doped carbon materials as supports for Fe-N-C catalysts, or even as "metal-free" (or "no metal added") catalysts in their own right, electrochemical analysis was performed. Cyclic voltammograms (CVs) measured in N_2 are shown in Figure 5 (a). These quasi-rectangular traces are typical for carbon materials with large surface area. The area within the plots for carbons synthesized using Method A are relatively small, corresponding to low double layer capacitance, in turn reflecting the relatively low surface area of these samples as measured by BET. Most of the sample's plots have similar area. However, two samples fabricated using Method B (i.e. N-C-B(1:3)$_{2,1000}$ and N-C-B(1:3)$_{5,1000}$) have much larger areas within the CV curves, suggesting higher double layer capacitance as a result of the much larger surface area. At potentials around 0.4 V_{RHE} and 0.65 V_{RHE} small peaks are observed in some of the plots, suggesting that oxygen-containing functional groups on the surface are undergoing redox transitions. Interestingly, sample N-C-A(1:1)$_{10,900}$ has lower capacitance, in agreement with the lower surface area and the unusual structure observed by SEM.

Figure 5 (b) shows linear sweep voltammograms measured in O_2 (after N_2 trace subtraction). Some activity for the oxygen reduction reaction is observed in all samples.

Nitrogen-doped carbons are already well-known to be ORR active even in the absence of iron or other transition metals.[38] However, this is usually attributed to production of hydrogen peroxide followed by reduction to water, in a 2+2 electron transfer step, rather than a direct 4 electron transfer which is preferred for use in practical applications.[39,10] For samples synthesized using Method A, the electrochemical current densities are all relatively low, reflecting the low surface area. The highest ORR activity for samples synthesized using Method A was N-C-A$(1:3)_{10,1000}$, and this informed the decision to choose the ratio of TEOA:EtOH = 1:3 for use in Method B. For samples synthesized using Method B, the highest ORR current density is observed for N-C-B $(1:3)_{5,1000}$, with very low ORR activity for the other samples. The large difference in LSV performance based only on the change in the heating rate in Method B is striking. This may reflect the higher oxygen content in N-C-B $(1:3)_{2,1000}$ as observed in XPS (also associated with the REDOX couple observed in the CV plots); the poor pore connectivity in N-C-B $(1:3)_{10,1000}$ as inferred from the lower mass limited current density; the smaller pore size of N-C-B $(1:3)_{5,1000}$ as observed in SEM; or the higher nitrogen content of N-C-B$(1:3)_{5,1000}$ as measured using XPS, potentially providing a higher density of metal-free ORR active sites. Despite these metal-free nitrogen-doped carbons not having sufficient activity to be useful catalysts in their own right, this electrochemical data suggests that

N-C-B $(1:3)_{5,1000}$ could be a suitable support material for the synthesis of Fe-N-C catalysts. This will be explored further in the following section.

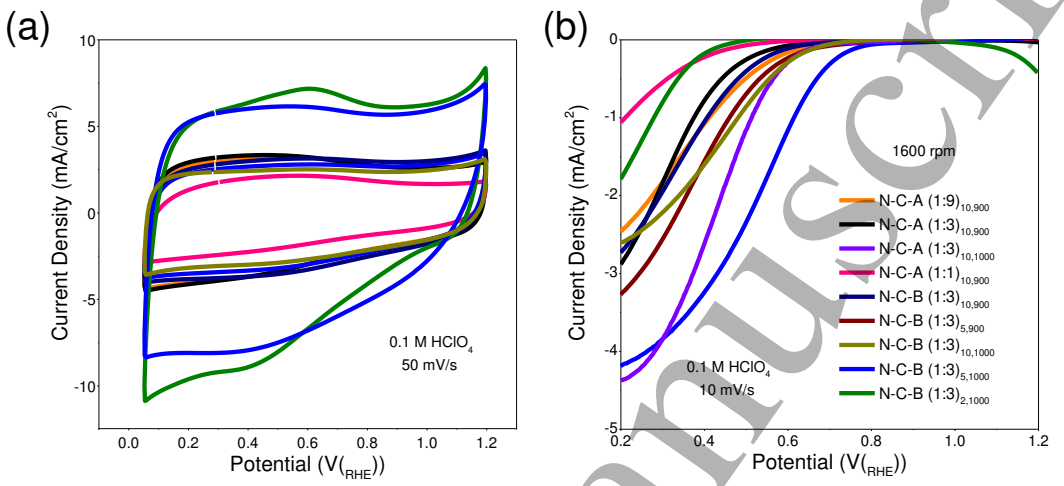

Figure 5: (a) Cyclic voltammograms (CVs), and (b) linear sweep voltammograms (LSVs) of the nitrogen-doped carbon foam materials.

3.6 Fe-N-C Electrocatalyst Synthesis

The most suitable candidate for use as an Fe-N-C support for electrocatalysis was selected with regards to optimized yield, nitrogen content, surface area, and electrochemical response, i.e. N-C-B $(1:3)_{5,1000}$ (herein re-named simply as N-C). As such, FeAc was infiltrated onto this nitrogen-doped carbon foam support, and then pyrolysis was carried out in NH_3 atmosphere, according to established protocols previously developed by Dodelet et al.[9,40] This Fe-N-C catalyst is compared with a commercially-sourced non-

PGM catalyst benchmark also based on a carbon, nitrogen and iron structure (NPC-2000, Pajarito Powder, transition metal content ~0.7%; nitrogen content 3.0%).[38]

The microstructure of the Fe-N-C catalyst is shown in the SEM images in Figure 6. The foam-type structure is retained, and the SEM images at low magnification are similar, as expected. However, at higher magnification, Figure 6(b), nanoparticles can be seen decorating the surface. In some regions, agglomerations of nanostructures are observed (Figure 6(c)), including carbon nanotubes grown via the catalytic action of Fe at elevated temperature.[41,42] Figure 6 (d) shows a higher magnification image of some of the nanoparticles, revealing a bright iron core encapsulated by carbon. The TEM image in Figure 6(e) shows a metallic Fe nanoparticle size of ~30 nm diameter. This is encapsulated by a few layers of graphitized carbon with a lattice spacing of ~0.35 nm, which is slightly larger than that of graphite (i.e. 0.335 nm). Selected area electron diffraction (SAED, Figure (6f)) confirmed that the nanoparticle core is metallic Fe, and the shell is graphitized carbon.

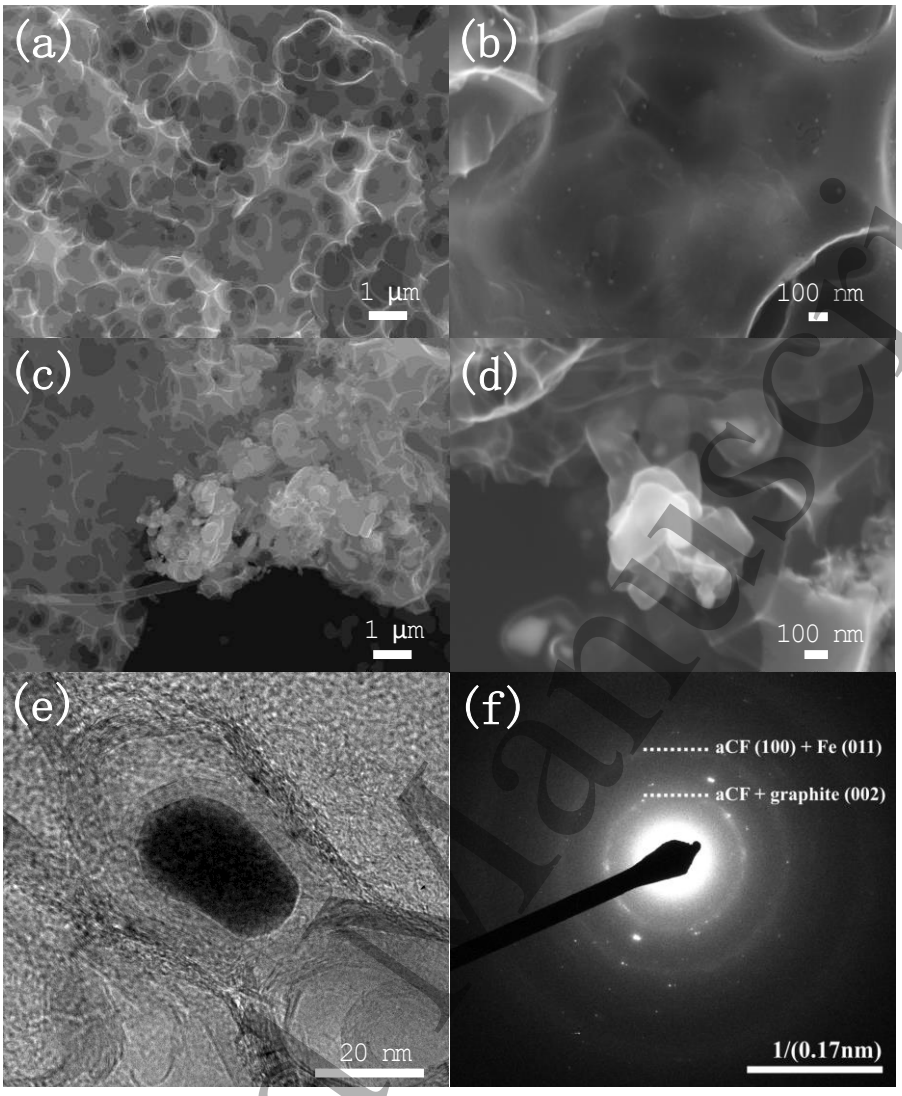

Figure 6: (a-d) SEM and (e, f) SAED and TEM images of the Fe-N-C catalyst.

The surface area of the Fe-N-C catalyst is 1600 m^2g^{-1}, as measured by BET, Figure (S5). Surprisingly, this is an increase compared to the un-decorated N-C support (1286 m^2g^{-1}). Fe-N-C has mixed Type I, Type II and Type H4 isotherms indicating a micro-mesoporous carbon with macroporous characteristics.[33,43] The total pore volume of N-C increases from 0.64 to 0.77 cm^3/g; the micropore volume does not significantly change; and the

mesopore volume increases from 0.12 to 0.26 cm^3/g after Fe decoration and heat treatment in ammonia (Table S2). This increase in surface area and porosity is attributed to the creation of additional carbon nanostructures as observed in Figure 6, and the action of NH_3 on the support, which is known to increase porosity. Meanwhile, the commercial NPC-2000 catalyst has a Type IV isotherm and a Type H1 hysteresis curve, strongly indicating a largely mesoporous material.[33] This clearly shows that the Fe-N-C and NPC-2000 materials are fundamentally different in microstructure.

The electrochemical performance of the Fe-N-C electrocatalyst using the optimized carbon support is summarized in Figure 7 and Table 3, and compared with the support material (N-C); platinum-decorated carbon black (Pt/C); and the NPC-2000 benchmark. This graph shows that the initial activity of the Fe-N-C catalyst using optimized nitrogen-doped carbon foam supports is reasonably high, with an onset potential of 0.88 V_{RHE}, a half-wave potential of 0.68 V_{RHE}, a mass diffusion limited current density of -5.5 mA/cm^2, a mass activity of 11.8 A/g (at 0.8 V_{RHE}); and an electron transfer number of 3.75 (Figure S8). The initial activity of Fe-N-C is slightly higher than the as-received NPC-2000 commercial catalyst, which has similar onset potential of 0.88 V_{RHE}, similar half-wave potential of 0.68 V_{RHE}, lower mass diffusion limited current density of -5.1 mA/cm^2; and

slightly higher electron transfer number. These measured values are slightly lower than those reported in the literature for NPC-2000,[44] which may be due to deactivation of the catalyst through exposure to oxygen and/or high atmospheric humidity levels, or differences in measurement protocols.

In general, the active sites are believed to largely reside in micropores, whilst mesopores contribute to enhanced mass transport.[45] As such, the co-existence of meso- and micropores in a suitable ratio has been reported to enhance mass diffusion in in activated carbon-based electrocatalysts.[43,46,47] Here, the mesopore to micropore volume ratios for Fe-N-C and NPC-2000 are 0.5 and 2, respectively, contrary to expected values for enhanced mass transport. Therefore, the improved mass transport in Fe-N-C must attributed to a different factor such as: the much larger total surface area (1607 vs 775 m^2/g); the higher mesopore/external surface area (656 vs 256 m^2/g); the higher microporous surface area (951 vs 519 m^2/g); the higher total pore volume (0.77 vs 0.70 cm^3/g).

The durability of these Fe-N-C catalysts against carbon corrosion was investigated using start-stop potential cycling (Figure S9). Whilst the initial activity of these catalysts is

promising, they quickly degrade under start-stop potential cycling. This may be due to the relatively amorphous nature of the carbon foam support (as observed by XRD), and/or the relatively high iron content, leading to carbon corrosion via the action of hydrogen peroxide. As such, in future work the iron loading will be optimised in future work.

However, the main conclusion of these electrochemical experiments is that careful optimization and selection of nitrogen-doped carbon foam supports can result in high-performance Fe-N-C electrocatalysts. This is attributed to high nitrogen content in the support, the large surface area, the large pore volume for effective mass diffusion, and screening of the metal-free supports using cyclic voltammetry. Another important conclusion of this work is that it is possible to decouple the introduction of nitrogen atoms in the support material and the introduction of iron atoms without compromising ORR activity. This is an advantage in comparison with more generalized Fe-N-C catalyst synthesis protocols in which the nitrogen and iron atoms are introduced in the same step. As such, this new protocol for synthesis of nitrogen-doped carbon foam supported Fe-N-C electrocatalysts could have important implications in the design and optimisation of new electrocatalysts.

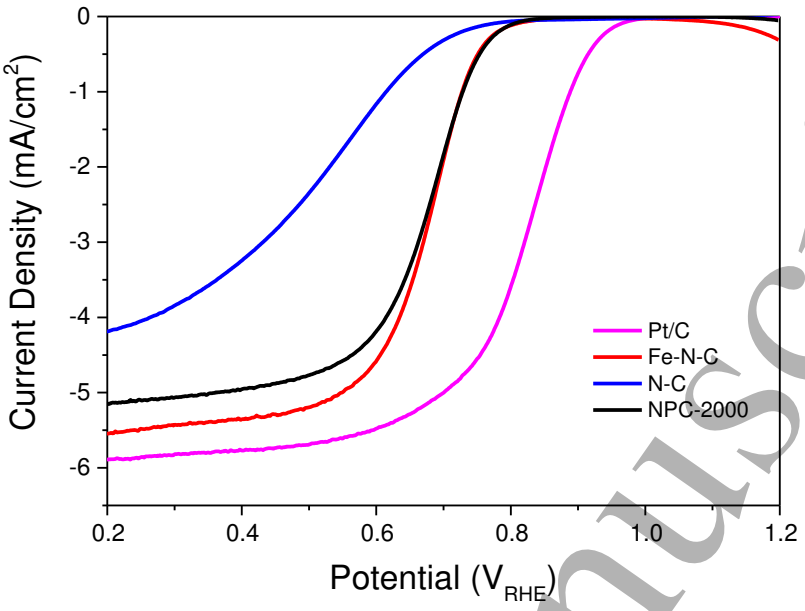

Figure 7: Linear sweep voltammograms (LSVs) of the Fe-N-C catalyst, compared with the support material N-C, NPC-2000 (Pajarito Powder), and Pt/C.

Table 3: Comparison of the electrochemical performance of the synthesized catalysts with conventional catalysts.

	Onset Potential (V_{RHE})	Half-Wave Potential (V_{RHE})	Mass Diffusion Limited Current Density (mA/cm^2)	Mass Activity (A/g @ 0.8 V_{RHE})
N-C	0.7	0.5	-4.2	0
Fe-N-C	**0.88**	**0.68**	**-5.56**	**11.8**
NPC-2000	0.88	0.68	-5.11	11.4
Pt/C	1.03	0.8	-5.91	70

3.7 Numerical Modelling

As discussed above, the difference in mesopore volume did not sufficiently explain the relatively high mass diffusion limited current density in the Fe-N-C sample. The very

large total surface area and increased total porosity were instead proposed as possible contributing factors. As such, the effect of surface area on mass transport was investigated using a simple model. To investigate the effect of microstructure on gas diffusion and mass transport through the electrocatalyst layer, two simple computational models were developed corresponding loosely to Fe-N-C and NPC-2000. A simple square symmetry approximation of the materials was made, based on physical characterization of the respective catalysts. The main physical difference between the different materials is the surface area, and this is reflected in the simulation. Since the surface area of Fe-N-C is approximately twice that of NPC-2000, the model takes this into account by changing the thickness of the carbon walls. As such, Fe-N-C is modelled with a primary pore size of 1000 nm, a wall thickness of 5 nm, a window size of 200 nm; and an electrocatalyst layer thickness of 11 μm. Meanwhile, NPC-2000 is modelled to have a primary pore size of 100 nm, a wall thickness of 10 nm, a window diameter of 20 nm, and an electrocatalyst layer thickness of 11 μm (Figure 8). The purpose of this calculation is to see how diffusive each structure is, so the only equation solved was for the conservation of mass for oxygen:

$$\nabla D \nabla C_{O_2} = 0 \qquad (1)$$

where C_{O_2} is the molar concentration of oxygen and D is the diffusion coefficient of oxygen (2.2×10^{-5} m^2/s). The boundary conditions used for the models are: a specified

concentration, calculated at 20°C and 1 bar, at the top edge of the domain; a convective flux, with a mass transfer coefficient of 1 m/s, at the bottom edge of the domain; and zero flux for the two sides of the domain. Equation (1) was solved using a finite element software, COMSOL Multiphysics® 5.2a. The computational domains were discretised and refined until mesh-independent solutions were obtained.

Figure 8 (c) and (d) show the respective distributions of oxygen concentration. For the given parameters and boundary conditions, the diffusion fluxes at the "outlet" of the electrocatalyst layers (i.e. the bottom edges of the domains) were calculated to be 7.43 and 7.16 mol/m^2/sec, respectively, representing a difference of around 4%. This confirms that mass diffusion is faster through the structure with a larger pore-to-wall thickness ratio, and this enhanced diffusion of oxygen could be one of the factors contributing to the higher mass transport limited current density observed in the experimental LSVs.

Whilst this simulation shows that surface area may have some influence on mass diffusion, this is only one of several potentially important factors. In future the model will be refined to investigate in more detail the accessibility of micropores and mesopores, the ratio of mesopores to micropores, and more fine-grained simulation of the microstructure.

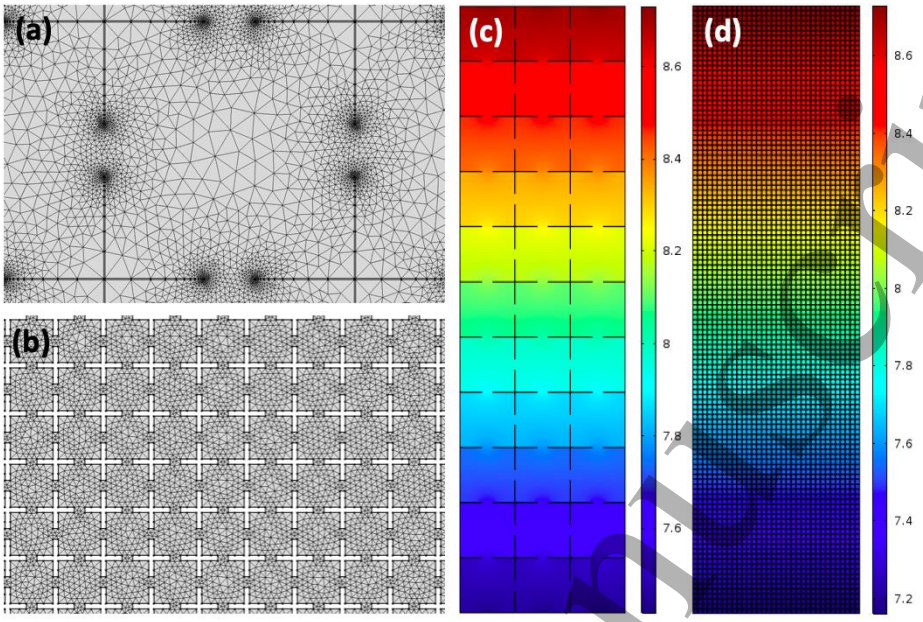

Figure 8: Meshed geometries for simulated approximations of (a) Fe-N-C and (b) NPC-2000 catalysts. For (a) the wall thickness is 5 nm, the pore size is 1 µm, and the window size is 200 nm. For (b) the wall thickness is 10 nm, the pore size is 100 nm and the window size is 20 nm. (c) and (d) show the simulated distribution of the molar oxygen concentration in Fe-N-C and NPC-2000, respectively.

Summary and Conclusions

In summary, we investigated how optimization of the carbon support can be used to improve the design of Fe-N-C ORR electrocatalysts. Template-free nitrogen-doped carbon foams with large surface area were developed using two different precursor synthesis protocols. Method A was a high pressure and high temperature solvothermal method previously demonstrated by our group. Method B was an ambient temperature-and-pressure solution-based method designed to make the process cheaper, more scalable, and safer. Method B successfully replicated the pore-structure of Method A, but increased

the surface area dramatically from ~500 to ~2500 m^2/g. The ratio of TEOA in the reaction was used to control the nitrogen content, surface area and microstructure of the final product. The heating rate during the first pyrolysis step was also found to dramatically affect the material properties. These support materials were then screened according to their electrochemical behaviour, and the most suitable was selected as a support for an Fe-based non-PGM catalyst, using FeAc as an iron source. The resulting catalyst had similar onset potential and mass activity, and slightly increased mass transport limited current density to a commercially-available non-PGM catalyst, NPC-2000. The efficient mass transport was attributed to the large pore-diameter-to-wall-thickness ratio in our samples, using multiphysics simulations. These results confirm that careful optimization and selective design of the pore size, surface area, nitrogen content, and heating rate of carbon-based supports can result in highly active Fe-N-C catalysts. In future work, we will further develop and optimize these supports to seek further improvements in activity, as well as performing durability studies and full cell testing.

4. Acknowledgements

The authors gratefully acknowledge the support of the Platform of Inter/Transdisciplinary Energy Research (Q-PIT), Kyushu University; the International Institute for Carbon

Neutral Energy Research (WPI-I2CNER), sponsored by the World Premier International Research Center Initiative (WPI), MEXT, Japan; and the Center-of-Innovation (COI) program, JST Japan. This work was also supported by a JSPS Bilateral Joint Research Projects grant; Grant-in-Aid for Scientific Research (B) Kakenhi Kiban B (19H02558); and the QDAI-JUMP Research Program, Kyushu University.

5. References

1. Marcinkoski, J., Spendelow, J., Wilson, A. & Papageorgopoulos, D. DOE Hydrogen and Fuel Cells Program Record - Fuel Cell System Cost - 2017. *J. Mech. Robot.* **9**, 1–9 (2017).

2. Dodelet, J.-P. The Controversial Role of the Metal in Fe- or Co-Based Electrocatalysts for the Oxygen Reduction Reaction in Acid Medium. in *Electrocatalysis in Fuel Cells* (eds. Shao, MinHiggins, D. & Chen, Z.) vol. 9 271–338 (Springer London, 2013).

3. Bezerra, C. W. B. *et al.* A review of Fe-N/C and Co-N/C catalysts for the oxygen reduction reaction. *Electrochim. Acta* **53**, 4937–4951 (2008).

4. Liu, R., Wu, D., Feng, X. & Müllen, K. Nitrogen-doped ordered mesoporous graphitic arrays with high electrocatalytic activity for oxygen reduction. *Angew.*

Chemie - Int. Ed. **122**, 2619–2623 (2010).

5. Serov, A. *et al.* Nano-structured non-platinum catalysts for automotive fuel cell application. *Nano Energy* **16**, 293–300 (2015).

6. Lalande, G. *et al.* Is nitrogen important in the formulation of Fe-based catalysts for oxygen reduction in solid. *Electrochim. Acta* **42**, 1379–1388 (1997).

7. Zitolo, A. *et al.* Identification of catalytic sites for oxygen reduction in iron- and nitrogen-doped graphene materials. *Nat. Mater.* **14**, 937–42 (2015).

8. Jaouen, F. *et al.* Recent advances in non-precious metal catalysis for oxygen-reduction reaction in polymer electrolyte fuel cells. *Energy Environ. Sci.* **4**, 114 (2011).

9. Michel Lefèvre, Eric Proietti, F. J. and J.-P. D. Iron-Based Catalysts with Improved Oxygen Reduction Activity in Polymer Electrolyte Fuel Cells. *Science (80-.).* **324**, 71–74 (2009).

10. Kattel, S., Atanassov, P. & Kiefer, B. A density functional theory study of oxygen reduction reaction on non-PGM Fe-Nx-C electrocatalysts. *Phys. Chem. Chem. Phys.* **16**, 13800–6 (2014).

11. Robson, M. H., Artyushkova, K., Patterson, W., Atanassov, P. & Hibbs, M. R. Non-platinum Carbon-Supported Oxygen Reduction Catalyst Ink Evaluation

Based on Poly(sulfone) and Poly(phenylene)-Derived Ionomers in Alkaline Media. *Electrocatalysis* (2013) doi:10.1007/s12678-013-0179-5.

12. Stephen M. Lyth, Y. Nabae, N. M. Islam, T. Hayakawa, S. Kuroki, M. Kakimoto, S. M. Solvothermal Synthesis of Nitrogen-Containing Graphene for Electrochemical Oxygen Reduction. *eJournal Surf. Sci. Nanotechnol.* **10**, 29–32 (2012).

13. Liu, J., Takeshi, D., Orejon, D., Sasaki, K. & Lyth, S. M. Defective Nitrogen-Doped Graphene Foam: A Metal-Free, Non-Precious Electrocatalyst for the Oxygen Reduction Reaction in Acid. *J. Electrochem. Soc.* **161**, F544–F550 (2014).

14. Lefe, M. Heat-Treated Fe / N / C Catalysts for O 2 Electroreduction : Are Active Sites Hosted in Micropores ? *J. Phys. Chem. B* **110**, 5553–5558 (2006).

15. Jaouen, F. *et al.* Cross-laboratory experimental study of non-noble-metal electrocatalysts for the oxygen reduction reaction. *ACS Appl. Mater. Interfaces* **1**, 1623–39 (2009).

16. Lyth, S. M. *et al.* Electrochemical Oxygen Reduction Activity of Carbon Nitride Supported on Carbon Black. *J. Electrochem. Soc.* **158**, B194 (2011).

17. Ferrandon, M. *et al.* Multitechnique Characterization of a Polyaniline − Iron −

Carbon Oxygen Reduction Catalyst. *J. Phys. Chem. C* **116**, 16001–16013 (2012).

18. Stariha, S., Serov, A., Halevi, B. & Atanassov, P. Non-PGM Membrane Electrode Assemblies: Optimization for Performance. in *2014 ECS and SMEQ Joint International Meeting (October 5-9, 2014)* (Ecs, 2014).

19. Lee, J., Kim, J. & Hyeon, T. Recent progress in the synthesis of porous carbon materials. *Adv. Mater.* **18**, 2073–2094 (2006).

20. Shao, M., Chang, Q., Dodelet, J.-P. & Chenitz, R. Recent Advances in Electrocatalysts for Oxygen Reduction Reaction. *Chem. Rev.* **116**, 3594–3657 (2016).

21. Rodríguez-Reinoso, F. The role of carbon materials in heterogeneous catalysis. *Carbon N. Y.* **36**, 159–175 (1998).

22. Stankovich, S. *et al.* Graphene-based composite materials. *Nature* **442**, 282–286 (2006).

23. Lyth, S. M. (2019). Doped and Decorated Carbon Foams for Energy Applications. in *Nakashima N. (eds) Nanocarbons for Energy Conversion: Supramolecular Approaches. Nanostructure Science and Technology.* 175–203 (Springer, Cham). doi:10.1007/978-3-319-92917-0_8.

24. Choucair, M., Thordarson, P. & Stride, J. a. Gram-scale production of graphene

based on solvothermal synthesis and sonication. *Nat. Nanotechnol.* **4**, 30–33 (2009).

25. S. M. Lyth, H. Shao, J. Liu, K. Sasaki, E. A. Hydrogen adsorption on graphene foam synthesized by combustion of sodium ethoxide. *Int. J. Hydrogen Energy* **39**, 376 (2014).

26. Liu, J., Takeshi, D., Sasaki, K. & Lyth, S. M. Defective Graphene Foam: A Platinum Catalyst Support for PEMFCs. *J. Electrochem. Soc.* **161**, F838–F844 (2014).

27. Speyer, L., Fontana, S., Ploneis, S. & Hérold, C. Influence of the precursor alcohol on the adsorptive properties of graphene foams elaborated by a solvothermal-based process. *Microporous Mesoporous Mater.* **243**, 254–262 (2017).

28. Lyth, S. M. *et al.* Solvothermal synthesis of superhydrophobic hollow carbon nanoparticles from a fluorinated alcohol. *Nanoscale* **7**, 16087–93 (2015).

29. Liu, J. *et al.* Nitrogen-Doped Carbon Foam as a Highly Durable Metal-Free Electrocatalyst for the Oxygen Reduction Reaction in Alkaline Solution. *Electrochim. Acta* **220**, 554–561 (2016).

30. Liu, J. *et al.* Metal-Free Nitrogen-Doped Carbon Foam Electrocatalysts for the

Oxygen Reduction Reaction in Acid Solution. *J. Electrochem. Soc.* **163**, F1049–F1054 (2016).

31. Takabatake, Y., Noda, Z., Lyth, S. M., Hayashi, A. & Sasaki, K. Cycle durability of metal oxide supports for PEFC electrocatalysts. *Int. J. Hydrogen Energy* **39**, 5074–5082 (2014).

32. Sasaki, K. *et al.* Part II Hydrogen Production. in *Hydrogen Energy Engineering - a Japanese perspective* 121–174 (Springer, 2016).

33. Thommes, M. *et al.* Physisorption of gases, with special reference to the evaluation of surface area and pore size distribution (IUPAC Technical Report). *Pure Appl. Chem.* **87**, 1051–1069 (2015).

34. *MicrotracBEL Corporation*. *BET Belsorp manual* vol. 2.3.4 (2014).

35. Sun, Z. *et al.* High-quality functionalized few-layer graphene: Facile fabrication and doping with nitrogen as a metal-free catalyst for the oxygen reduction reaction. *J. Mater. Chem. A* **3**, 15444–15450 (2015).

36. White, G. C. & Raynor, S. T. The effect of phenothiazine and non-phenothiazine inhibitors of calmodulin on platelet calcium fluxes. *Biochem. Biophys. Res. Commun.* **104**, 1066–1072 (1982).

37. Chung, H. T. *et al.* Direct atomic-level insight into the active sites of a high-

performance PGM-free ORR catalyst. *Science (80-.).* **357**, 479–484 (2017).

38. Mufundirwa, A. *et al.* Durability of template-free Fe-N-C foams for electrochemical oxygen reduction in alkaline solution. *J. Power Sources* **375**, 244–254 (2018).

39. Gewirth, A. A. & Thorum, M. S. Electroreduction of dioxygen for fuel-cell applications: Materials and challenges. *Inorg. Chem.* **49**, 3557–3566 (2010).

40. Jaouen, F., Charreteur, F. & Dodelet, J. P. Fe-Based Catalysts for Oxygen Reduction in PEMFCs. *J. Electrochem. Soc.* **153**, A689 (2006).

41. Schaper, A. K., Hou, H., Greiner, A. & Phillipp, F. The role of iron carbide in multiwalled carbon nanotube growth. *J. Catal.* **222**, 250–254 (2004).

42. Huang, S., Dai, L. & Mau, A. W. H. Patterned growth and contact transfer of well-aligned carbon nanotube films. *J. Phys. Chem. B* **103**, 4223–4227 (1999).

43. Yeh, C. L., Hsi, H. C., Li, K. C. & Hou, C. H. Improved performance in capacitive deionization of activated carbon electrodes with a tunable mesopore and micropore ratio. *Desalination* **367**, 60–68 (2015).

44. Serov, A., Artyushkova, K. & Atanassov, P. Fe-N-C oxygen reduction fuel cell catalyst derived from carbendazim: Synthesis, structure, and reactivity. *Adv. Energy Mater.* **4**, 1–7 (2014).

45. Li, J. C. *et al.* Hierarchically porous Fe-N-doped carbon nanotubes as efficient electrocatalyst for oxygen reduction. *Carbon N. Y.* **109**, 632–639 (2016).

46. Choi, J. Y. *et al.* Is the rapid initial performance loss of Fe/N/C non precious metal catalysts due to micropore flooding? *Energy Environ. Sci.* **10**, 296–305 (2017).

47. Proietti, E. *et al.* Iron-based cathode catalyst with enhanced power density in polymer electrolyte membrane fuel cells. *Nat. Commun.* **2**, (2011).